Published for SISSA by Springer

Received: *February 7, 2025*
Accepted: *March 23, 2025*
Published: *April 24, 2025*

Analytic next-to-leading order Yukawa and Higgs boson self-coupling corrections to $gg \to HH$ at high energies

Joshua Davies,[a] **Kay Schönwald**,[b] **Matthias Steinhauser**[c] **and Hantian Zhang**[d]

[a] *Department of Mathematical Sciences, University of Liverpool, Liverpool, L69 3BX, U.K.*
[b] *Physik-Institut, Universität Zürich, Winterthurerstrasse 190, 8057 Zürich, Switzerland*
[c] *Institut für Theoretische Teilchenphysik, Karlsruhe Institute of Technology (KIT), Wolfgang-Gaede Straße 1, 76131 Karlsruhe, Germany*
[d] *PSI Center for Neutron and Muon Sciences, 5232 Villigen PSI, Switzerland*

E-mail: J.O.Davies@liverpool.ac.uk, kay.schoenwald@physik.uzh.ch, matthias.steinhauser@kit.edu, hantian.zhang@psi.ch

Abstract: We consider electroweak corrections to Higgs boson pair production, taking into account the top quark Yukawa and Higgs boson self couplings. Using differential equations we compute a deep expansion of all master integrals in the high-energy limit and present analytic results for the two-loop box-type form factors. We show that precise numerical results can be obtained even for relatively small values of the Higgs boson transverse momentum. We compare against recent numerical results and find good agreement.

Keywords: Electroweak Precision Physics, Higgs Production, Higgs Properties, Higher Order Electroweak Calculations

ArXiv ePrint: 2501.17920

https://doi.org/10.1007/JHEP04(2025)193

Contents

1 Introduction

Higgs boson pair production is one of the most promising processes to obtain more insight into the scalar sector of the Standard Model. For this reason it will play a central role in the Large Hadron Collider's (LHC) physics program in the coming years. From the theory side it is important to provide precise predictions for this process.

At the LHC, Higgs boson pair production is dominated by the gluon fusion production process. The NLO QCD corrections [1–4] turn out to be large, with a K factor close to two. In this work we compute a subset of the electroweak corrections and construct analytic expansions in the high-energy limit with explicit dependence on the kinematic variables and mass parameters. Our results have the advantage that their numerical evaluation is fast and flexible; in particular, it is straightforward to use different renormalization schemes and change the values of the particle masses.

There are a number of publications in the literature in which electroweak corrections to Higgs boson pair production have been considered. Leading m_t^4 and m_t^2 terms have been considered in ref. [5]. The contribution to $gg \to HH$ with four top quark Yukawa couplings has been computed in ref. [6] in the high-energy limit. It has been shown that the inclusion of about 100 expansion terms provides stable results, even for rather small values of the Higgs boson transverse momentum. The first complete calculation of the top quark contribution to $gg \to HH$, including all Standard Model contributions, has been performed in ref. [7] in the large-m_t limit, where five expansion terms were presented. Numerical results for all Standard Model contributions are available from ref. [8]. Analytic results for all factorizing contributions have been published in ref. [9] and in refs. [10–12] the contributions from diagrams with top quarks and Higgs bosons have been computed numerically. In this work we consider the same set of contributions as in ref. [11] and compute the form factors in

JHEP04(2025)193

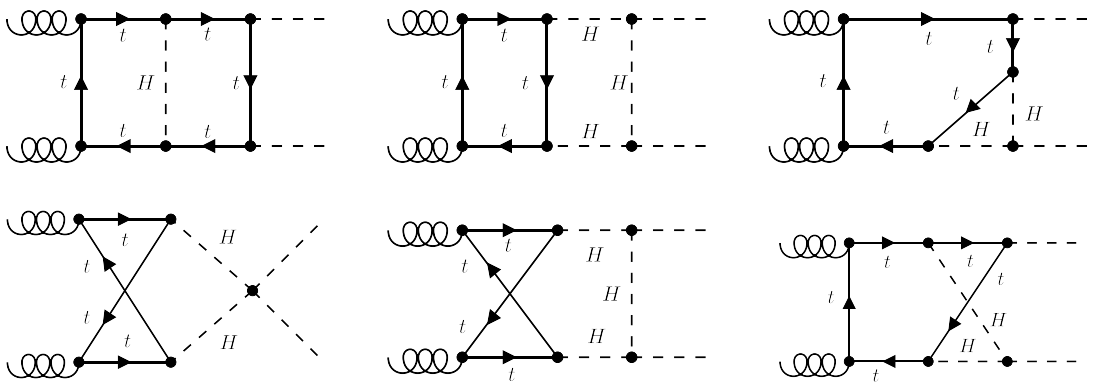

Figure 1. Sample Feynman diagrams. Solid, dashed and curly lines represent top quarks, Higgs bosons and gluons, respectively.

the high-energy limit, including terms up to m_t^{120}. We restrict the discussion in this paper to the more complicated box-type form factors.

In the past, deep expansions in the high-energy limit have proven to be valuable ingredients for a number of processes. For example, the QCD corrections to $gg \to HH$ [13, 14] have been combined with the numerical approach of refs. [1, 2] in ref. [4] and with a forward-scattering approximation in refs. [15, 16]. High-energy expansions of $gg \to ZH$ [17] and $gg \to ZZ$ [18] have also been successfully combined with expansions around the forward-scattering limit [15, 19–21]. In each case the high-energy expansion was a crucial input to be able to describe the whole phase space. The results of refs. [13, 14] were also useful input into the analysis of ref. [22] where the high-energy behaviour of the $gg \to HH$ amplitude has been investigated in a resummation framework.

Concerning electroweak corrections to $gg \to HH$, such expansions have been computed in ref. [6] for the leading Yukawa contributions. Two approaches concerning the hierarchies of the scales were considered: (A) $s, t \gg m_t^2 \gg (m_H^{\text{int}})^2, (m_H^{\text{ext}})^2$ and (B) $s, t \gg m_t^2 \approx (m_H^{\text{int}})^2 \gg (m_H^{\text{ext}})^2$, where m_H^{ext} denotes the mass of the final-state Higgs bosons and m_H^{int} denotes the mass of the Higgs bosons propagating in the loops. For practical reasons, in this work only approach (B) can be applied to the contributions involving Higgs boson self couplings. In contrast to ref. [6] where the non-trivial asymptotic expansion of approach (A) produces only two fairly simple sub-diagrams, here many more sub-diagrams are involved.

In this paper we consider the contributions to the form factors from the two-loop box diagrams involving top quarks and a Higgs boson. Sample Feynman diagrams are shown in figure 1, and we can classify the diagrams according to their coupling structure: y_t^4, $y_t^2 g_3^2$, $y_t^3 g_3$, $y_t^2 g_4$, where y_t, g_3 and g_4 denote the Yukawa coupling to the top quark and the triple and quartic Higgs boson self couplings, respectively. These contributions have been computed in ref. [11] using numerical methods. Below we will perform detailed comparisons of the individual contributions. The high-energy expansion of the y_t^4 contribution has already been computed in ref. [6].

The outline of this paper is as follows. In section 2 we discuss the conventions used in the present paper. Afterwards, in section 3, we present technical details about the generation of

JHEP04(2025)193

the amplitude and the approximations we apply, and the calculation of the master integrals in the high-energy expansion. In section 4 we show numerical results for the master integrals and form factors, analyse the convergence of the expansions, and compare our results to those of ref. [11]. We conclude in section 5.

2 Conventions

The amplitude for the process $g(q_1)g(q_2) \to H(q_3)H(q_4)$ can be defined by two scalar matrix elements $\mathcal{M}_1$ and $\mathcal{M}_2$ via

$$\mathcal{M}^{ab} = \varepsilon_{1,\mu}\varepsilon_{2,\nu}\mathcal{M}^{\mu\nu,ab} = \varepsilon_{1,\mu}\varepsilon_{2,\nu}\delta^{ab}\left(\mathcal{M}_1 A_1^{\mu\nu} + \mathcal{M}_2 A_2^{\mu\nu}\right), \tag{2.1}$$

where a and b are adjoint colour indices and the two Lorentz structures are given by

$$\begin{aligned} A_1^{\mu\nu} &= g^{\mu\nu} - \frac{1}{q_{12}} q_1^\nu q_2^\mu, \\ A_2^{\mu\nu} &= g^{\mu\nu} + \frac{1}{p_T^2 q_{12}}\left(q_{33} q_1^\nu q_2^\mu - 2q_{23} q_1^\nu q_3^\mu - 2q_{13} q_3^\nu q_2^\mu + 2q_{12} q_3^\mu q_3^\nu\right), \end{aligned} \tag{2.2}$$

with $q_{ij} = q_i \cdot q_j$. The scalar matrix elements can furthermore be split into "triangle" and "box" form factors

$$\begin{aligned} \mathcal{M}_1 &= X_0\, s \left(\frac{3m_H^2}{s - m_H^2} F_{\text{tri}} + F_{\text{box1}}\right), \\ \mathcal{M}_2 &= X_0\, s\, F_{\text{box2}}, \end{aligned} \tag{2.3}$$

with

$$X_0 = \frac{G_F}{\sqrt{2}} \frac{\alpha_s(\mu)}{2\pi} T, \tag{2.4}$$

where $T = 1/2$, μ is the renormalization scale and G_F is the Fermi constant.

All momenta are defined incoming, so the Mandelstam variables are given by

$$s = (q_1 + q_2)^2, \qquad t = (q_1 + q_3)^2, \qquad u = (q_2 + q_3)^2, \tag{2.5}$$

with

$$q_1^2 = q_2^2 = 0, \qquad q_3^2 = q_4^2 = m_H^2, \qquad s + t + u = 2m_H^2. \tag{2.6}$$

Later we will also use the scattering angle θ and the transverse momentum of the Higgs bosons in the center-of-mass frame, which are given by

$$\begin{aligned} p_T^2 &= \frac{ut - m_H^4}{s}, \\ t &= m_H^2 - \frac{s}{2}\left(1 - \cos\theta \sqrt{1 - \frac{4m_H^2}{s}}\right). \end{aligned} \tag{2.7}$$

We extend the perturbative expansion of the form factors given in eq. (8) of ref. [6] to

$$\begin{aligned} F_{\text{box}} &= F_{\text{box}}^{(0)} + \frac{\alpha_s(\mu)}{\pi} F_{\text{box}}^{(1,0)} + \frac{\alpha_t}{\pi} F_{\text{box}}^{(0,y_t^4)} + \sqrt{\frac{\alpha_t}{\pi}\frac{\hat{\lambda}}{\pi}} F_{\text{box}}^{(0,y_t^3 g_3)} + \frac{\hat{\lambda}}{\pi} F_{\text{box}}^{(0,y_t^2 g_3^2)} + \frac{\hat{\lambda}}{\pi} F_{\text{box}}^{(0,y_t^2 g_4)} + \cdots \\ &= F_{\text{box}}^{(0)} + \frac{\alpha_s(\mu)}{\pi} F_{\text{box}}^{(1,0)} + \frac{\alpha_t}{\pi} F_{\text{box}}^{(0,\alpha_t)}, \end{aligned} \tag{2.8}$$

JHEP04(2025)193

with

$$F_{\text{box}}^{(0,\alpha_t)} = F_{\text{box}}^{(0,y_t^4)} + \frac{m_H}{m_t} F_{\text{box}}^{(0,y_t^3 g_3)} + \frac{m_H^2}{m_t^2} F_{\text{box}}^{(0,y_t^2 g_3^2)} + \frac{m_H^2}{m_t^2} F_{\text{box}}^{(0,y_t^2 g_4)} \tag{2.9}$$

where

$$\begin{aligned} \hat{\lambda} &= \frac{\lambda}{\pi} = \frac{1}{\pi} \frac{m_H^2}{2v^2} \,, \\ \alpha_t &= \frac{\alpha\, m_t^2}{2 \sin^2 \theta_W\, m_W^2} \,. \end{aligned} \tag{2.10}$$

α is the fine structure constant, θ_W is the weak mixing angle and v is the Higgs vacuum expectation value. In eq. (2.8), $F^{(0)}$ is the leading one-loop contribution (which contains two Yukawa couplings) and $F^{(1,0)}$ represents the two-loop QCD corrections. The remaining terms refer to the different contributions considered in this paper. We have introduced the quantities y_t, g_3 and g_4 to distinguish the contributions from the Higgs-top quark Yukawa and the three- and four-Higgs boson couplings. In this paper we only consider the one-particle irreducible box diagrams which is indicated by the subscript "box". We will use the F_{box1} and F_{box2} notation of eq. (2.3) to distinguish between the Lorentz structures for these form factors. From the technical point of view the triangle and reducible contributions are much simpler and are not considered in this paper. Note that we count $F_{\text{box}}^{(0,y_t^2 g_4)}$ as a "box" contribution since it does not have an intermediate Higgs propagator. However, from the technical point of view it is a triangle contribution; in particular it has no dependence on p_T. For this reason it only contributes to F_1 but not to F_2.

Of the four electroweak two-loop contributions defined in eq. (2.8), only $F_{\text{box}}^{(0,y_t^4)}$ develops ultra-violet $1/\epsilon$ poles.[1] These cancel against the contribution from the top quark mass counterterm (see ref. [6] for details); the remaining three contributions are finite after summing all bare two-loop diagrams. Note that there are no infrared singularities present in any of these coupling structures.

3 Technicalities

3.1 Generation of the amplitude

For the generation of the analytic expressions for the form factors in terms of Lorentz-scalar Feynman integrals we use a well-tested setup with is based on `qgraf` [23] for the generation of the amplitude, `tapir` [24] for the translation to `FORM` [25] notation and the generation of auxiliary files for processing the integral topologies, and on `exp` [26, 27] for the mapping of each Feynman diagram onto a minimal subset of the integral topologies from `tapir`. In all integral families all internal lines have the same mass: m_t. The internally propagating Higgs bosons are expanded around m_t as a series in $\delta' = 1 - (m_H^{\text{int}}/m_t)^2$ as described in ref. [6]. In the final results we switch to the expansion parameter $\delta = 1 - m_H^{\text{int}}/m_t$ by using the relation

$$\delta' = \delta\,(2 - \delta) \,, \tag{3.1}$$

and expanding in δ again, since it shows better convergence properties (as e.g. described in ref. [28]).

[1] In table 3 of ref. [11] there are poles for "$g_3 g_t^3$" since there also triangle contributions are included.

JHEP04(2025)193

The computation of the amplitude is performed with the in-house `FORM` code "`calc`", which applies projectors to obtain the form factors, takes traces and expresses the final result in terms of scalar integrals of the integral families selected by `exp`. In this step we also perform the expansion of all Higgs boson propagators such that in the final results we have terms up to order δ^3. At this point the scalar integrals depend on the variables $\{s, t, m_H^{\text{ext}}, m_t\}$; δ is only present in the integral coefficients.

The next step is to expand in the final state Higgs boson mass which is encoded in the relation of the external momenta $\{q_1, q_2, q_3\}$ to the Mandelstam variables and m_H^{ext}. For the expansion at the level of the integrands it is convenient to use `LiteRed` [29, 30] and to perform the expansion for each of the scalar integrals. We generate `FORM id` statements which are applied to the summed expressions for the form factors. Now the remaining scalar integrals depend only on $\{s, t, m_t\}$.

Next, we perform a reduction to master integrals within each topology using `Kira` [31, 32], followed by an additional reduction of all 1224 master integrals among all topologies to yield a final minimal set of 168 master integrals, 28 of which are non-planar. We made some effort to optimize the integral basis to remove spurious ϵ poles (where $D = 4 - 2\epsilon$) in the master integral coefficients in the amplitude, particularly for master integrals in the top-level sectors. This was only partially successful, thus in intermediate steps it was necessary to compute some master integrals to order ϵ^1, in terms of some transcendental weight 5 objects which ultimately cancel in the amplitude. This provides a strong consistency check of our reduction and basis minimization procedures.

3.2 Computation of the master integrals

The analytic calculation of the master integrals in the high-energy region is more involved compared to the QCD-like master integrals considered in refs. [13, 14, 16, 33], due to the larger number of massive propagators. Nevertheless, for their calculation similar methods can be used. In total we find 168 master integrals, 140 of these are planar integrals which have already been considered in ref. [6] for the leading Yukawa corrections to double Higgs production. For the current calculation some of the planar master integrals from the lower sectors had to be extended to $\mathcal{O}(\epsilon)$ due to spurious poles in the amplitude which we were not able to remove. The remaining 28 master integrals are non-planar integrals with six and seven massive internal lines and their calculation is significantly more complex than the calculation of the planar master integrals.

Let us briefly recap the strategy for the calculation of the planar master integrals used in ref. [6] applied to all 168 master integrals, before discussing the modifications which were necessary for the non-planar case. The first step is to insert a power-log ansatz for each master integral, assuming the hierarchy $s, |t| \gg m_t^2$,

$$I_n = \sum_{i,j,k} C_{ijk}^{(n)}(s,t)\, \epsilon^i \left(m_t^2\right)^j \log(m_t^2)^k \tag{3.2}$$

into the system of differential equations with respect to m_t^2.

$$\partial_{m_t^2} \mathbf{I} = \mathbf{A}(s, t, m_t^2, \epsilon)\, \mathbf{I}\,. \tag{3.3}$$

JHEP04(2025)193

This yields a system of linear equations for the expansion coefficients $C_{ijk}^{(n)}(s,t)$, which are still functions of s and t. By solving the system of linear equations with `Kira` [32] and `FireFly` [34, 35], we can reduce the large number of independent coefficients to a small number of boundary conditions which need to be fixed by a direct calculation. In total, for the planar and non-planar master integrals, we need to fix 543 boundary conditions (i.e. 543 functions of the type $C_{ijk}^{(n)}(s,t)$). In the planar cases we obtain them by means of Mellin-Barnes integrals and symbolic summation [6]. This approach has recently been partially automated in the package `AsyInt` [36], which employs the packages `Asy` [37], `MB` [38], `HarmonicSums` [39–50] and `Sigma` [51, 52].

As for the case of the QCD-like master integrals, in the fully-massive case the non-planar master integrals also develop both even and odd power terms in the expansion for small m_t (the high-energy region), the latter are not covered by the ansatz in eq. (3.2). Since the equation systems for the even and odd power expansions completely decouple, we treat them separately. In fact, for the odd-power contribution we can apply the same strategy as for the planar master integrals and compute the boundary functions $C_{ijk}^{(n)}(s,t)$ directly. In contrast to the planar master integrals, here we encounter square roots in the Mandelstam variables ($\sqrt{-t/s}$ and $\sqrt{1+t/s}$). Although the dependence on t of the odd power expansion is rather simple, we find involved numerical coefficients. One of them is given by

$$\begin{aligned} c_Z &= \int_0^\infty \int_0^\infty \frac{\mathrm{d}\alpha_1\,\mathrm{d}\alpha_2}{\sqrt{\alpha_1\,\alpha_2\,(\alpha_1+\alpha_2+1)\,(\alpha_2\alpha_1+\alpha_1+\alpha_2)}} \\ &= \sum_{k=0}^{\infty} \frac{\Gamma^4(k+1/2)}{\pi\Gamma^2(k+1)\Gamma(2k+1)} \Big(8\log(2) + 6S_{-1}(2k)\Big) \\ &= 4\sqrt{3}\,K^2\left(\frac{1}{2}-\frac{\sqrt{3}}{4}\right) \\ &= 17.695031908454309764234228747255048751062059438637\ldots\,, \end{aligned} \tag{3.4}$$

where $S_{-1}(n) = \sum_{i=1}^{n}(-1)^i/i$ and $K(z)$ is the complete elliptic function of the first kind given by

$$K(z) = \int_0^1 \mathrm{d}t \frac{1}{\sqrt{1-t^2}\sqrt{1-zt^2}}\,. \tag{3.5}$$

We were able to determine the closed-form solution with the help of `HarmonicSums` and the `PSLQ` algorithm [53], where the former was able to perform the symbolic summation on parts of eq. (3.4). In the amplitude also a second elliptic constant appears

$$\begin{aligned} c_{Z_2} &= \sum_{k=0}^{\infty} \frac{\Gamma^4(k+1/2)}{\pi\Gamma^2(k+1)\Gamma(2k+1)} \left(\frac{k\ln(2)}{2(1+k)} - \frac{1}{16(1+k)^2} + \frac{3k}{8(1+k)} S_{-1}(2k)\right) \\ &= \left(1+\frac{1}{\sqrt{3}}\right)\pi + \left(2+\frac{17}{4\sqrt{3}}\right) K^2 \left(\frac{1}{2}-\frac{\sqrt{3}}{4}\right) - 4\sqrt{3}E^2\left(\frac{1}{2}-\frac{\sqrt{3}}{4}\right) \\ &= -0.189114824528715301590514265622885511401742116540\ldots\,, \end{aligned} \tag{3.6}$$

JHEP04(2025)193

where $E(z)$ is the complete elliptic integral of the second kind which reads

$$E(z) = \int_0^1 \mathrm{d}t \frac{\sqrt{1-zt^2}}{\sqrt{1-t^2}}\,. \tag{3.7}$$

The most difficult boundary constant for the odd-m_t terms is a seven-line non-planar master integral, evaluated up to $\mathcal{O}(\epsilon\, m_t)$.

For the even-power contributions of the non-planar master integrals this strategy, however, becomes too complicated since a large number of non-trivial one-, two- and three-dimensional Mellin-Barnes integrals have to be solved. In the following we describe the strategy which we have applied for these contributions.

We use the expression of the even-power expansion of the master integrals in terms of the 543 boundary conditions and insert them into the differential equation with respect to t

$$\partial_t \mathbf{I} = \mathbf{M}(s,t,m_t^2,\epsilon)\,\mathbf{I}\,, \tag{3.8}$$

where $\mathbf{M}(s,t,m_t^2,\epsilon)$ is still exact in all variables. After expanding this equation in terms of m_t^2 and ϵ, and comparing coefficients on both sides of the equation, we arrive at a system of coupled linear differential equations with respect to t for the 543 boundary conditions, which we group into the vector $\vec{C}(t)$ (here and in the following we set $s=1$, since its dependence can be recovered using dimensional analysis):

$$\partial_t \vec{C}(t) = \mathbf{M}_t(t)\vec{C}(t)\,. \tag{3.9}$$

The 543×543 dimensional matrix $\mathbf{M}_t(t)$ now only depends on t, since expansions for small ϵ and m_t^2 have already been performed. We solve this system of differential equations as outlined in ref. [54], i.e. we decouple the system of differential equations into higher order differential equations for individual boundary conditions and solve these with the help of `HarmonicSums`. In order to fully solve the differential equation we need to provide integration constants for the limit $t \to 0$. In contrast to our previous approach these are just numbers, and depend neither on m_t nor on t. We obtain them with Mellin-Barnes techniques, which simplify since we do not need to reconstruct the full t dependence. Note that there are non-trivial boundary integrals that require computing the exact u-dependence even in the $t \to 0$ limit. These are solved using the `Expand&Fit` module of `AsyInt`.

Before actually performing the calculation of the integration constants, we use the full t dependence of $\vec{C}(t)$ and use the crossing symmetries between the master integrals to reduce the number of necessary integration constants. It turns out that this step leads to a reduction by a factor of 3 in the number of integration constants which need to be calculated explicitly. For example, it turns out that deeper expansion terms in m_t are not needed and it is sufficient to provide the seven-line non-planar master integral up to $\mathcal{O}(\epsilon\, m_t^0)$ instead of $\mathcal{O}(\epsilon\, m_t^2)$, which was necessary in the previous approach. Note that we also recalculate all planar master integrals in this way and find complete agreement with our previously obtained results [6]. We also reproduce the $\mathcal{O}(\epsilon^0 m_t^0)$ terms of the seven-line non-planar master integral from ref. [36].

We provide the analytic expressions for the master integrals expanded up to m_t^{100} in an ancillary file to this publication [55]. It turns out that also in the fully massive case the

JHEP04(2025)193

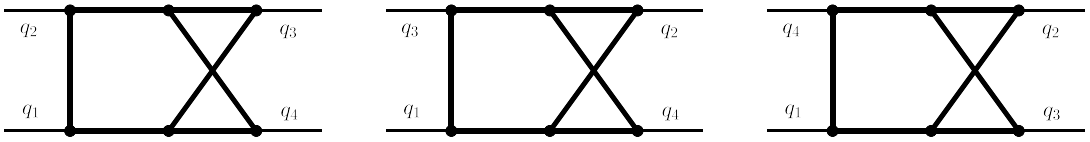

$I_{150} = G_{52}(1,1,1,1,1,1,1,0,0)$ $I_{157} = G_{53}(1,1,1,1,1,1,1,0,0)$ $I_{164} = G_{54}(1,1,1,1,1,1,1,0,0)$

Figure 2. Sample top-level master integrals, where all internal lines have the same mass m_t and all external lines are massless.

function space of the high-energy expansion is spanned by a subset of harmonic polylogarithms with the letters 0 and 1. During the calculation we had to introduce several integration constants for which we were not able to determine closed expressions:

$$\begin{aligned} c_6 &= -66.606101552505094835462532159285032068889118084828\ldots\,, \\ c_7 &= 8.245227873742566544491578437011715020871425138609\ldots\,, \\ c'_Z &= -46.834387660276172083477753650852669635341902837429\ldots\,, \\ c'_{Z_2} &= -0.127899599664440859067122151592372323466385155017\ldots\,. \end{aligned} \tag{3.10}$$

Note that the constants c_6, c_7, c'_Z and c'_{Z_2} enter the master integrals only at $\mathcal{O}(\epsilon)$ and cancel in the physical amplitudes. In the ancillary file we provide numerical evaluations with 600 significant digits for completeness. The physical amplitudes thus turn out to depend on the following set of transcendental numbers

$$\left\{ \sqrt{3},\, \log(3),\, \pi,\, c_Z,\, c_{Z_2},\, \psi^{(1)}\left(\frac{1}{3}\right),\, \zeta_3,\, \mathrm{Im}\left[\mathrm{Li}_3\left(\frac{i}{\sqrt{3}}\right)\right] \right\}, \tag{3.11}$$

while individual master integrals additionally depend on

$$\left\{ \mathrm{Im}\left[\mathrm{Li}_3\left(\frac{i\sqrt{3}+1}{4}\right)\right],\, \mathrm{Im}\left(G_{0,0,0,r_2}(1)\right),\, \mathrm{Im}\left(G_{0,1,1,r_4}(1)\right),\, \zeta_5,\, c_6,\, c_7,\, c'_Z,\, c'_{Z_2} \right\}, \tag{3.12}$$

where G denotes multiple polylogarithms, see e.g. ref. [56], with the additional letters $r_2 = (1-\sqrt{3}i)/2$, $r_4 = -r_2^*$ of the sixth root of unity. A full determination of the basis up to weight six can be found in refs. [43, 57].

4 Results

4.1 Master integrals

We first discuss the quality of the high-energy expansion at the level of individual master integrals. As examples, we use the seven-line (top sector) master integrals of the three non-planar integral families shown in figure 2. All internal lines have the mass m_t and all external particles are massless. For all integrals we have an expansions up to m_t^{120}.

In figure 3 we show results for the ϵ^0 coefficient of these integrals as a function of $\sqrt{s}$, for fixed values of $p_T = 300\,\mathrm{GeV}$, $p_T = 200\,\mathrm{GeV}$ and $p_T = 100\,\mathrm{GeV}$. For the internal mass we use $m_t = 173\,\mathrm{GeV}$ and the renormalization scale is set to $\mu^2 = s$. Although the external masses are zero we use $m_H = 125\,\mathrm{GeV}$ in the relations between s, t, u and p_T. We follow ref. [18] and

JHEP04(2025)193

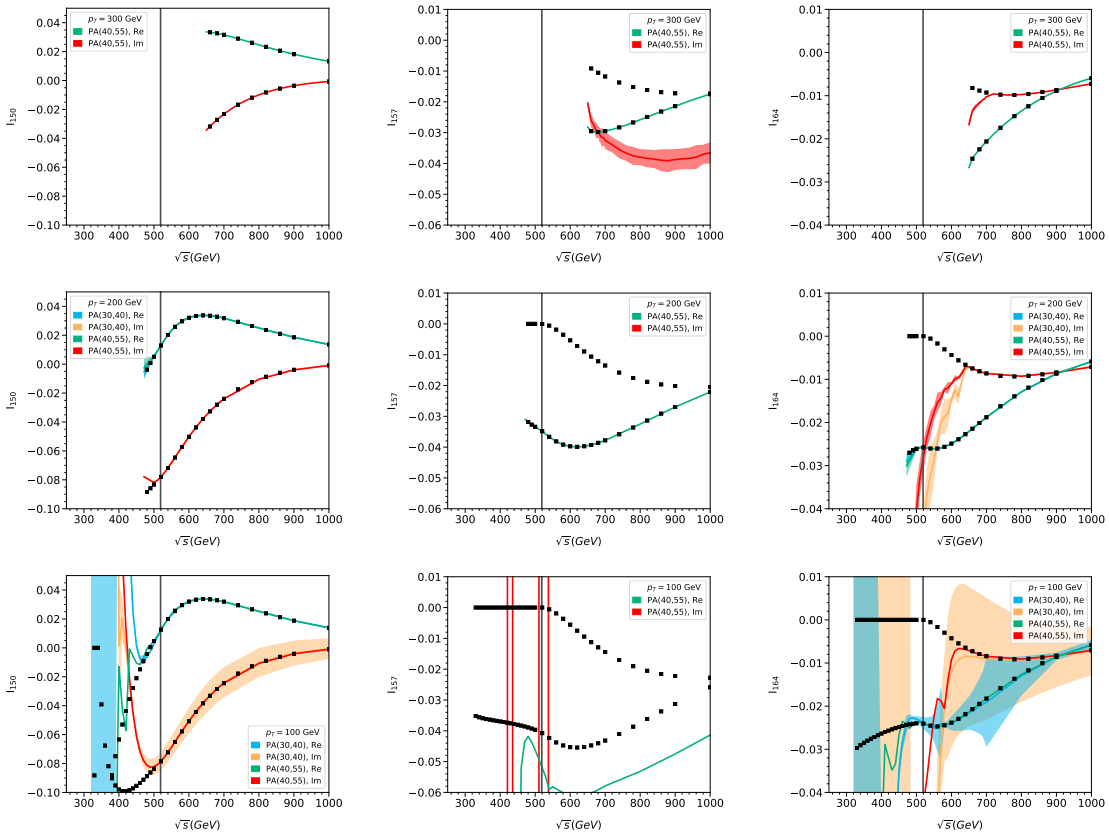

Figure 3. Dependence on $\sqrt{s}$ for real and imaginary parts for the three top-level master integrals shown in figure 2 for $p_T = 300\,\text{GeV}$ (top row) $p_T = 200\,\text{GeV}$ (middle row) and $p_T = 100\,\text{GeV}$ (bottom row). We multiply the integrals by m_t^6 such they are dimensionless. The coloured lines and bands correspond to the results based on the Padé-improved high-energy expansion and the black dots to the numerical results obtained with `AMFlow`. No uncertainty bands are shown for I_{157} for $p_T = 100\,\text{GeV}$ and $p_T = 200\,\text{GeV}$. The gray vertical line indicates the threshold at $3m_t = 519\,\text{GeV}$.

construct the so-called "pole distance re-weighted" Padé approximants and the corresponding uncertainties (see section 4 of [18] for a detailed discussion). We combine odd and even powers of m_t [16] and construct all possible Padé approximants $[n/m]$ in the variable m_t^2 which include at least terms of order $(m_t^2)^{N_\text{low}}$ and at most of order $(m_t^2)^{N_\text{high}}$, i.e. we have

$$N_\text{low} \leq n + m \leq N_\text{high} \quad \text{and} \quad N_\text{low} \leq n + m - |n - m|\,. \tag{4.1}$$

For demonstration purposes we show in figure 3 results for the real and imaginary parts of the three master integrals for $\{N_\text{low}, N_\text{high}\} = \{30, 40\}$ and $\{N_\text{low}, N_\text{high}\} = \{40, 55\}$. We show both the central values and the uncertainty bands as estimated by the Padé procedure. The results are compared to numerical results obtained with `AMFlow` [58, 59], which have no visible uncertainties. We plot the results from the kinematically allowed threshold up to $\sqrt{s} = 1000\,\text{GeV}$.

For I_{150} (left-hand column) we observe good agreement between the Padé approximation and the numerical results for each value of p_T. Deviations are only observed for $p_T = 100\,\text{GeV}$ when $\sqrt{s}$ is below the three-particle cut at $3m_t = 519\,\text{GeV}$, shown as a vertical grey line.

JHEP04(2025)193

It is impressive that for even lower values of p_T (not shown in figure 3) good results are obtained for $\sqrt{s} \gtrsim 3m_t$.

In the case of I_{164} (right-hand column) good agreement is observed for the real part for all values of p_T displayed, which has a similar quality as in the case of I_{150}. For larger values of $\sqrt{s}$ the imaginary part also shows a good behaviour, however for $\sqrt{s} \lesssim 650\,\text{GeV}$ we observe a significant deviation of the Padé result, though its uncertainty band remains rather small. This value of $\sqrt{s}$ is not directly connected to any of the cuts of the diagram which are at $2m_t = 346\,\text{GeV}$ for $\sqrt{-u}$ and $3m_t = 519\,\text{GeV}$ in all three Mandelstam variables. It appears that the non-planar diagram has pseudo-thresholds which cause this behaviour. The advantage of the deep expansions in m_t is clearly seen in the bottom-right plot where $p_T = 100\,\text{GeV}$ has been chosen. The sizeable uncertainty bands which are still present for lower-order Padé results largely disappear for the high-order Padé approximations.

For I_{157} we observe good agreement for the real part for $p_T = 300\,\text{GeV}$ and $p_T = 200\,\text{GeV}$. However, already for $p_T = 300\,\text{GeV}$ the imaginary part shows an unstable behaviour and does not agree with the numerical results. The situation becomes worse for lower values of p_T where the uncertainty bands fill the whole plot area. For this reason we refrain from showing it. For $p_T = 100\,\text{GeV}$ also the real part of the Padé approximant does not agree with the numerical result.

Although at first sight the three master integrals shown in figure 3 look similar, their convergence properties are very different. The three diagrams each have three-particle cuts in all of the Mandelstam variables s, t and u. However, the main difference is that each of them has only one two-particle cut either in $\sqrt{s}$ (I_{150}), $\sqrt{-t}$ (I_{157}) or $\sqrt{-u}$ (I_{164}), which seems to be responsible for the observed convergence behaviour. For example, for the kinematic values chosen in figure 3 $\sqrt{-t}$ is close to, or even below, $2m_t$. This might be the reason for the poor convergence behaviour of I_{157}. For lower p_T and lower $\sqrt{s}$ additionally $\sqrt{-u}$ becomes close to $3m_t$, which might explain the observed behaviour of I_{164}.

In the phase-space region covered in figure 3 the master integral I_{157} shows bad convergence properties. In order to show that in the high-energy region it reproduces the numerical results from `AMFlow` we show in figure 4 the results of the three top-level master integrals for fixed scattering angles θ, which is obtained from eq. (2.7). We choose three scattering angles, $\pi/2$, $\pi/3$ and $\pi/4$. For I_{150} we observe good agreement for all angles up to the threshold for $\sqrt{s} = 3m_t$. This is also true for the real part of I_{164} whereas the imaginary part starts to deviate from the exact result for $\sqrt{s} \lesssim 700 - 800\,\text{GeV}$. In the high-energy region good results are also obtained for I_{157} which slightly deteriorate for smaller scattering angles.

In summary, the comparison of the Padé-improved results for the master integrals to numerical results obtained with `AMFlow` provides confidence for the correctness of the analytic high-energy expansions of the master integrals.

Note that out of our four two-loop form factors introduced in eq. (2.8), only $F_{\text{box}}^{(0,y_t^3 g_3)}$ receives contributions from the families G_{53} and G_{54}. Thus, we anticipate worse convergence properties for (the imaginary part of) $F_{\text{box}}^{(0,y_t^3 g_3)}$ compared to the remaining three form factors. In general, we expect precise predictions for all form factors in the region $p_T \gtrsim 300\,\text{GeV}$.

To demonstrate the quality of the Padé predictions within the radius of convergence we compare in table 1 results for the master integral I_{150} for selected values of p_T and $\sqrt{s}$

JHEP04(2025)193

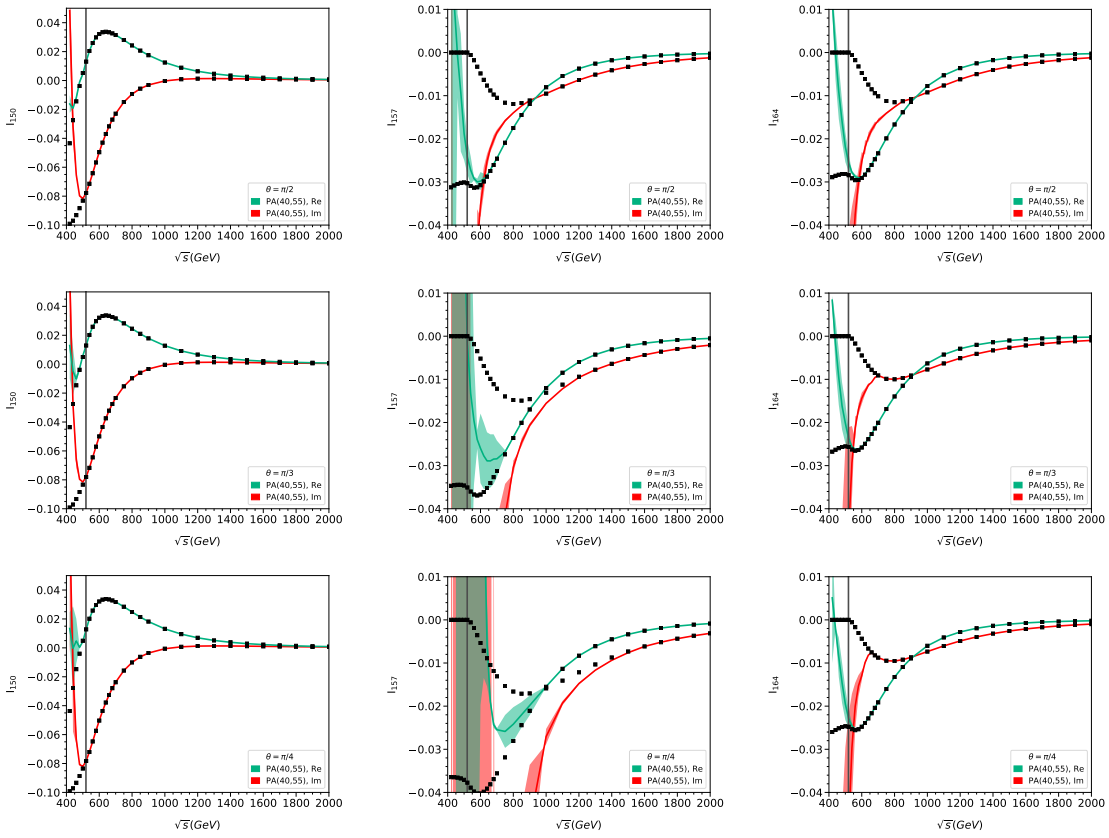

Figure 4. Dependence on $\sqrt{s}$ for finite real and imaginary parts for the three top-level master integrals shown in figure 2 for scattering angles $\theta = \pi/2$ (top row) $\theta = \pi/3$ (middle row) and $\theta = \pi/4$ (bottom row). We multiply the integrals by m_t^6 such they are dimensionless. The coloured lines and bands correspond to the results based on the Padé-improved high-energy expansion and the black dots to the numerical results obtained with `AMFlow`. The gray vertical line indicates the threshold at $3m_t = 519\,\text{GeV}$.

to the results obtains with `AMFlow`. It is impressive that for large values of $\sqrt{s}$ and p_T the Padé method can reproduce more than 15 significant digits of the exact result. Even for $p_T = 200\,\text{GeV}$ and $\sqrt{s} = 520$, which is very close to the $3m_t = 519\,\text{GeV}$ threshold, we obtain three significant digits, and for $p_T = 100\,\text{GeV}$ still two. In all cases the uncertainty estimate covers the exact result.

In a next step we study the quality of the expansion in the external Higgs boson mass and in δ. In table 2 we show results for the scalar non-planar integral $I_{150}^{(y_t^3\, g_3)}$ depicted in figure 5 for selected values of p_T and $\sqrt{s}$. We provide both the central values and the Padé uncertainties and compare to the numerical results from `AMFlow` (which always has an negligible uncertainty). For reference we also provide results for the expansion in the external Higgs boson mass and δ'.

For higher values of p_T and/or $\sqrt{s}$ the Padé uncertainty is negligible and we find agreement at the percent level or better. This remaining difference can be attributed to the neglected terms in δ and m_H. For smaller values of p_T or values of $\sqrt{s}$ close to the production threshold

JHEP04(2025)193

p_T (GeV)	$\sqrt{s}$ (GeV)	Padé-improved results for I_{150} up to $\mathcal{O}(m_t^{110})$	`AMFlow` for I_{150}
100	520	0.012231(840) −0.07818(670) i	0.012616 −0.07848 i
100	1000	0.013853(180) −0.000986(146) i	0.013856 −0.000990 i
200	520	0.01290367(594) −0.07801176(26) i	0.01292119 −0.07801270 i
200	1000	0.01363961528613(121) −0.00086534770114(198) i	0.01363961528606 −0.00086534770126 i
300	660	0.0333941347347566(83) −0.0317960435292528(113) i	0.0333941347347600 −0.0317960435292533 i
300	1000	0.013302917959524752 −0.0006827034768774084 i	0.013302917959524752 −0.0006827034768774084 i

Table 1. Padé-improved and numerical results for selected values of p_T and $\sqrt{s}$ for the ϵ^0 term of the master integral I_{150}. For the Padé approximation, we choose $\{N_{\text{low}}, N_{\text{high}}\} = \{40, 55\}$. The shown uncertainties are from the Padé procedure. We multiply this integral by m_t^6 such that it is dimensionless.

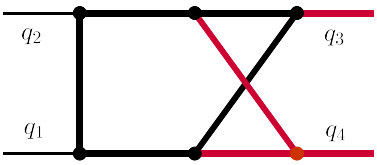

Figure 5. Scalar Feynman integral $I_{150}^{(y_t^3\, g_3)}$ of family G_{52} where thick black lines have mass m_t and thick red lines have mass m_H. The external lines with momenta q_1 and q_2 are massless.

$(3m_t)$ the Padé uncertainty becomes larger; it covers well the exact result. It is impressive that even for $p_T = 100\,\text{GeV}$ and $\sqrt{s} = 520\,\text{GeV}$ we can reproduce one digit in the exact result. In all cases the expansion in δ is slightly better than the expansion in δ'.

To conclude this subsection we want to stress that: (1) the Padé method as applied within the region of convergence is a precision tool and (2) the uncertainty estimate is reliable. (3) For the form factors we expect agreement with the exact result within 1% or better if p_T is sufficiently large, say above 200 to 300 GeV, with the exception of $\text{Im}(F_{\text{box}}^{(0,y_t^3 g_3)})$, where p_T needs to be above about 500 GeV.

We provide results for all 168 master integrals expanded up to order m_t^{100} in the supplementary material to the paper which can be downloaded from [55].

JHEP04(2025)193

p_T (GeV)	$\sqrt{s}$ (GeV)	$I_{150}^{(y_t^3 g_3)}$ up to $\mathcal{O}(m_H^4\,\delta'^3)$	$I_{150}^{(y_t^3 g_3)}$ up to $\mathcal{O}(m_H^4\,\delta^3)$	`AMFlow` for $I_{150}^{(y_t^3 g_3)}$
100	520	0.0640(35) $-0.1457(124)\,\mathrm{i}$	0.0667(37) $-0.1472(119)\,\mathrm{i}$	0.06982 $-0.14878\,i$
100	1000	0.02084(50) $+0.00240(21)\,\mathrm{i}$	0.02105(52) $+0.00254(21)\,\mathrm{i}$	0.02115 $+0.00265\,i$
200	520	0.06502(9) $-0.14501(8)\,\mathrm{i}$	0.06826(67) $-0.14648(1)\,\mathrm{i}$	0.07034 $-0.14728\,\mathrm{i}$
200	1000	$0.02038 + 0.00254\,\mathrm{i}$	$0.02058 + 0.00268\,\mathrm{i}$	$0.02066 + 0.00279\,\mathrm{i}$
300	660	$0.068325 - 0.038190\,\mathrm{i}$	$0.069487 - 0.038045\,\mathrm{i}$	$0.070304 - 0.037667\,\mathrm{i}$
300	1000	$0.019667 + 0.002729\,\mathrm{i}$	$0.019841 + 0.002864\,\mathrm{i}$	$0.019915 + 0.002973\,\mathrm{i}$
400	840	$0.034359 - 0.002381\,\mathrm{i}$	$0.034717 - 0.002176\,i$	$0.034897 - 0.001972\,\mathrm{i}$
400	1200	$0.009551 + 0.003347\,\mathrm{i}$	$0.009616 + 0.003420\,\mathrm{i}$	$0.009640 + 0.003468\,\mathrm{i}$

Table 2. Results for the ϵ^0 term of the scalar non-planar integral $I_{150}^{(y_t^3\,g_3)}$ (see figure 5) which enters $F_{\mathrm{box}}^{(0,y_t^3\,g_3)}$. The expansion in m_H and δ' respectively m_H and δ is compared to the numerical result form `AMFlow` for various values of p_T and $\sqrt{s}$. The uncertainties shown are from the Padé procedure.

4.2 Form factors

This subsection is devoted to analytic and numerical results of the form factors. We study in particular the quality of the various expansions. Let us start with the analytic structure of our result. As an illustration we show in the following the two leading terms in the high-energy expansion of the form factor $F_{\mathrm{box1}}^{(0,y_t^2 g_3^2)}$. They are of order m_t^2 and m_t^3, respectively. We have

$$
\begin{aligned}
F_{\mathrm{box1}}^{(0,y_t^2 g_3^2)} = -m_H^2 \Bigg\{ & m_t^2 \Bigg[\frac{18 L_m^2}{s^2} + L_m \Bigg(-\frac{9\pi^2}{s^2} - \frac{18t}{s^2(s+t)} H_{0,0} - \frac{18}{s^2} H_{0,1} - \frac{18}{s^2} H_{1,0} \\
& - \frac{18(s+t)}{s^2 t} H_{1,1} \Bigg) + \pi^2 \Bigg(-\frac{27}{2s^2} + \frac{9t}{2s^2(s+t)} H_0 - \frac{9(s+t)}{2s^2 t} H_1 \Bigg) \\
& - \frac{18t}{s^2(s+t)} H_{0,0} - \frac{18}{s^2} H_{0,1} - \frac{18}{s^2} H_{1,0} - \frac{18(s+t)}{s^2 t} H_{1,1} + \frac{18t}{s^2(s+t)} H_{0,0,0} \\
& + \frac{9}{s^2} H_{0,0,1} + \frac{9}{s^2} H_{0,1,0} - \frac{9}{st} H_{0,1,1} - \frac{9}{s(s+t)} H_{1,0,0} - \frac{9}{s^2} H_{1,0,1} - \frac{9}{s^2} H_{1,1,0} \\
& - \frac{18(s+t)}{s^2 t} H_{1,1,1} - \frac{9t}{s^2(s+t)} \zeta_3 + \mathrm{i}\pi \Bigg(L_m \Bigg(\frac{18}{s^2} + \frac{18}{s(s+t)} H_0 + \frac{18}{st} H_1 \Bigg) \\
& \times \frac{18}{s(s+t)} H_0 + \frac{18}{st} H_1 - \frac{9}{s(s+t)} H_{0,0} + \frac{9}{st} H_{0,1} - \frac{9}{s(s+t)} H_{1,0} + \frac{9}{st} H_{1,1} \\
& - \frac{3\pi^2}{2s(s+t)} \Bigg) \Bigg] + \mathrm{i} m_t^3 \sqrt{\frac{-t}{s+t}} \frac{9\pi^2 (5 c_Z + 16 c_{Z_2})}{8 t s^{3/2}} + \mathcal{O}(m_t^4) \Bigg\} \\
& + \mathcal{O}(m_H^4) + \mathcal{O}(\delta)\,,
\end{aligned}
\tag{4.2}
$$

JHEP04(2025)193

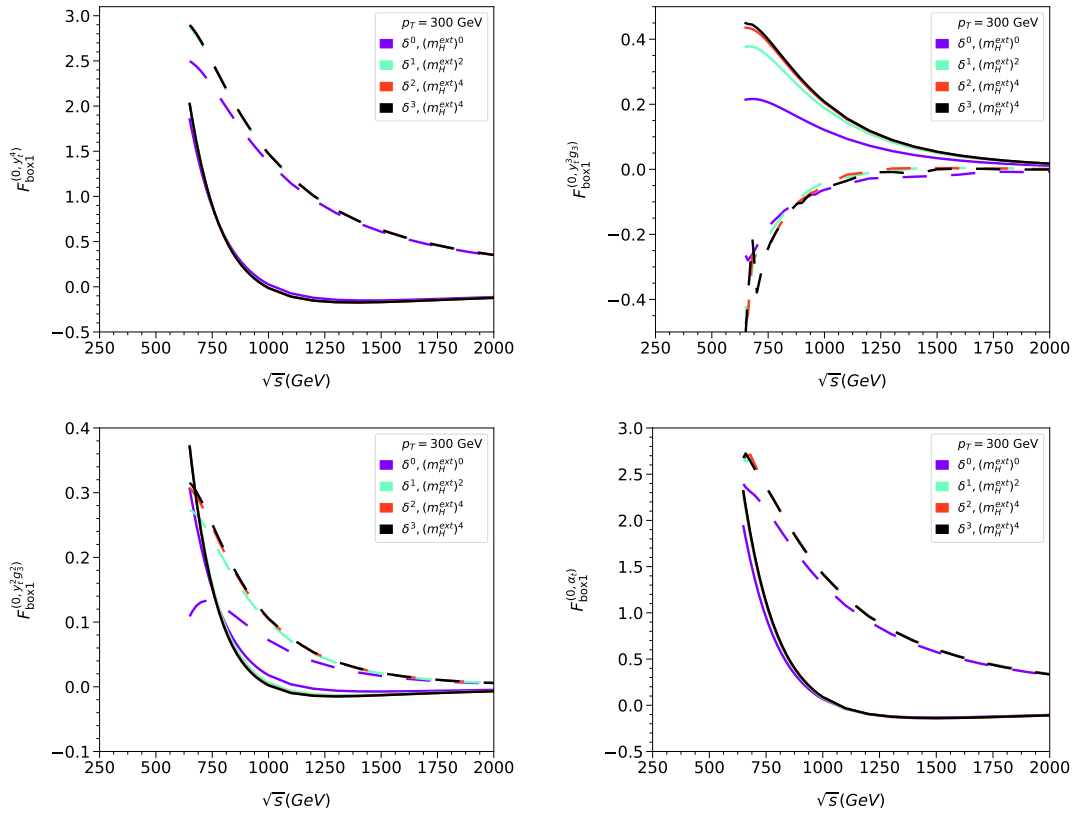

Figure 6. Form factors as a function of $\sqrt{s}$ for $p_T = 300\,\text{GeV}$. Real and imaginary parts are shown as solid and dashed curves.

with $L_m = \log(m_t/\sqrt{s})$ and $H_{\vec{w}} \equiv H_{\vec{w}}(-t/s)$ are harmonic polylogarithms. Note that the overall factor m_H^2 arises due to the way we write the prefactor in eq. (2.8). It is not counted in our expansion in m_H^{ext}. We see the general feature that the even powers in m_t can be expressed in terms of harmonic polylogarithms and rather well known polylogarithmic constants, while the odd powers also contain the elliptic constants c_Z and c_{Z_2}. Analytic results for all form factors introduced in eq. (2.8) can be found in the supplementary material [55].

Next we turn to the numerical analysis. For the input parameters we choose $m_t = 173\,\text{GeV}$, $m_H^{\text{int}} = m_H^{\text{ext}} = m_H = 125\,\text{GeV}$ and set $\mu^2 = s$. Furthermore, we fix p_T and then show the dependence on $\sqrt{s}$. As discussed for the individual master integrals in the previous subsection we construct, for each phase-space point, the Padé-improved result which consists of a central value and an uncertainty. If not stated otherwise we include expansion terms between m_t^{80} and m_t^{100} to construct the Padé approximants. A detailed analysis of the one-loop results of the form factors can be found in ref. [6]. In the following we will thus concentrate on the bare two-loop expressions. Furthermore, we will restrict the discussion to F_{box1}; we also have results for F_{box2} (see ref. [55]). Note that results for $F^{(0,y_t^4)}_{\text{box1}}$ can also be found in ref. [6], although only for the renormalized form factor.

In figures 6 and 7 we study the expansions in m_H^{exp} and δ for $p_T = 300\,\text{GeV}$ and $p_T = 200\,\text{GeV}$, respectively. We show results for the real and imaginary parts for the

JHEP04(2025)193

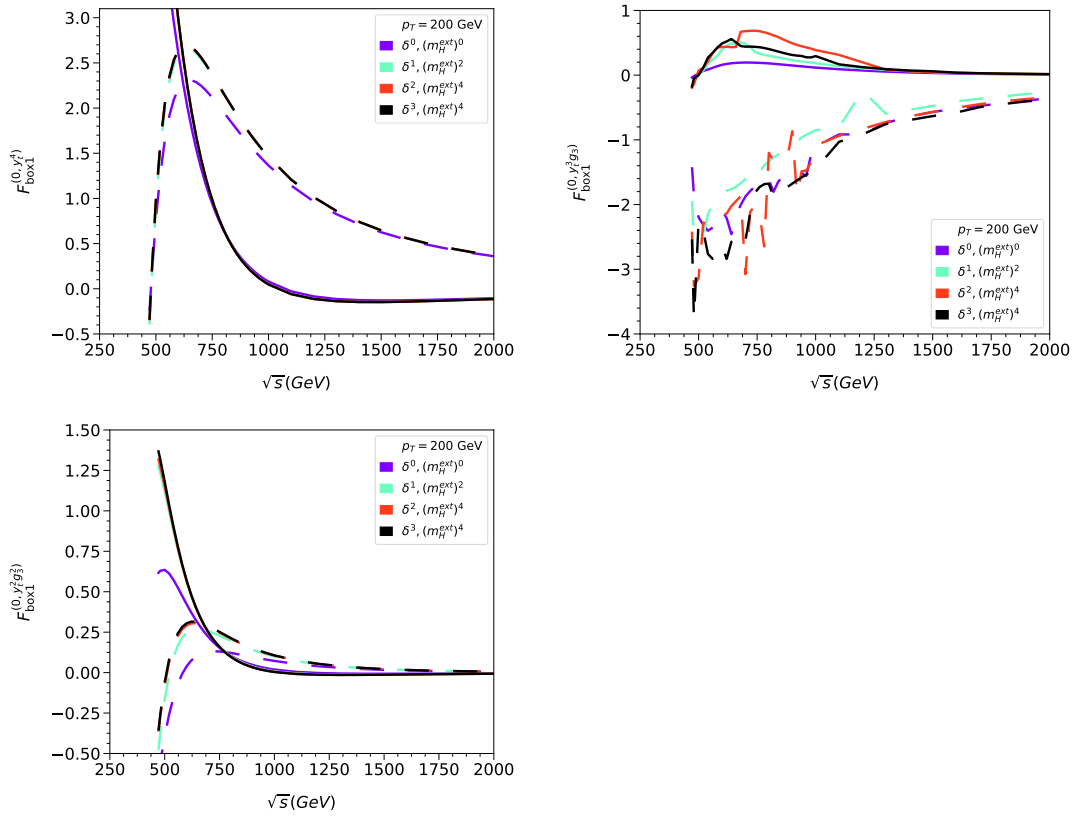

Figure 7. Same as figure 6 but for $p_T = 200\,\text{GeV}$.

individual form factors as solid and dashed lines, respectively. In figure 6 also results for the sum as given in eq. (2.8) are shown. Note that in the approximations labelled "δ^n" in the plot legend, all higher order δ terms are set to zero for each of the expansion terms in m_H^{exp}.

For $p_T = 300\,\text{GeV}$ we observe a rapid convergence in both expansion parameters for all form factors. In all cases the red and black curves more-or-less lie on top of each other.

For $p_T = 200\,\text{GeV}$ (see figure 7) the form factors $F^{(0,y_t^4)}_{\text{box1}}$ and $F^{(0,y_t^2 g_3^2)}_{\text{box1}}$ behave very similarly as for $p_T = 300\,\text{GeV}$. However, for $F^{(0,y_t^3 g_3)}_{\text{box1}}$ we observe an unstable behaviour, in particular for the imaginary part. This is most likely due to the families G_{53} and G_{54} (see the discussion in section 4.1) which do not contribute to $F^{(0,y_t^4)}_{\text{box1}}$ and $F^{(0,y_t^2 g_3^2)}_{\text{box1}}$. We refrain from showing the total contribution in this case, which inherits the instability from $F^{(0,y_t^3 g_3)}_{\text{box1}}$. Note that instabilities come together with large uncertainty bands (which, for clarity, are not shown in figure 7) from the Padé method.

In figure 8 we show the real and imaginary parts of the form factors F_{box1} for values of p_T between 200 GeV and 500 GeV. Note that in all cases we plot both the central value and the uncertainty bands obtained by the Padé approach. Each curve starts at the lowest value for $\sqrt{s}$ allowed by kinematic constraints. Stable results are obtained for $F^{(0,y_t^4)}_{\text{box1}}$ and $F^{(0,y_t^2 g_3^2)}_{\text{box1}}$ where, even for smaller values of p_T, the uncertainty bands are not visible. As expected

JHEP04(2025)193

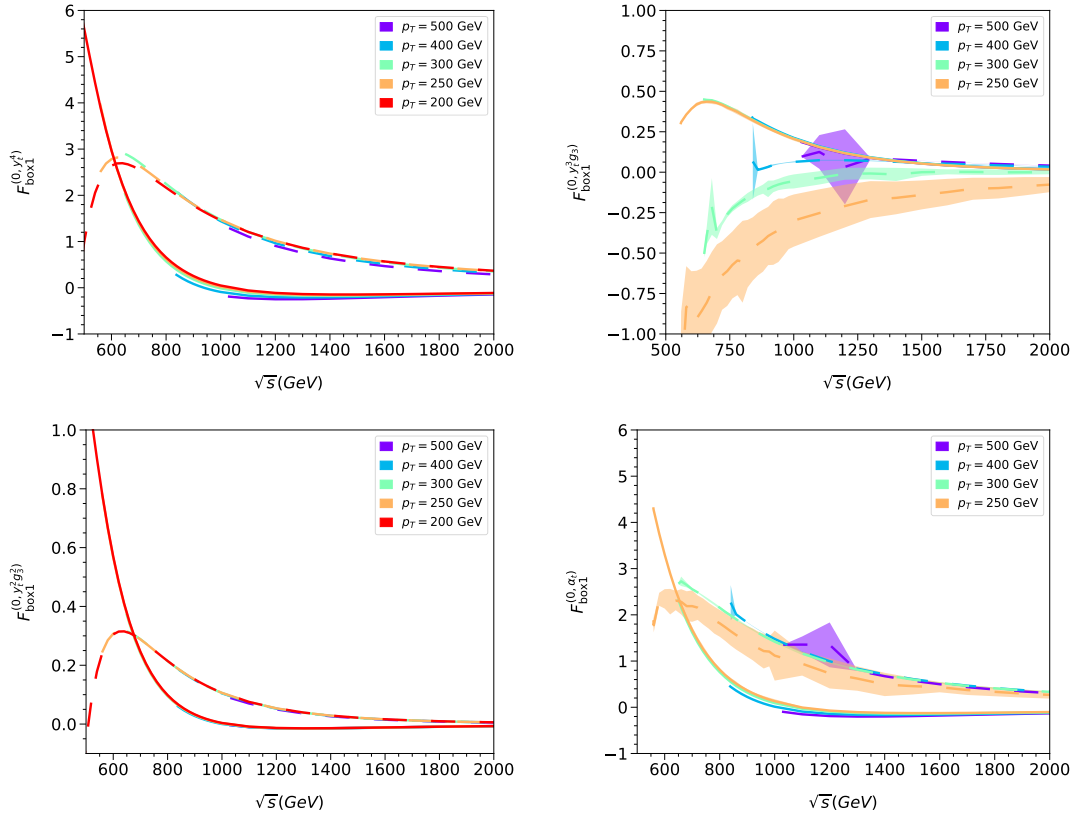

Figure 8. Form factors as a function of $\sqrt{s}$ for different value of p_T. Solid and dashed lines refer to the real and imaginary parts.

from the previous considerations, $F^{(0,y_t^3 g_3)}_{\text{box1}}$ becomes unstable below $p_T \approx 300\,\text{GeV}$ whereas for larger values of $\sqrt{s}$ and p_T precise results are obtained.

In our practical calculation we generate these deep analytic expansions of the sum of all coupling structures split into the 12 pieces of the m_H and δ expansions. The gzipped version of each part is about 40 MB. Currently we perform the numerical evaluation in `Mathematica`. Here inserting the kinematics takes of the order of a minute. The subsequent construction of the Padé approximants takes about a second. We plan to implement our results into a `C++` code and expect that the total evaluation time will reduce to a few milliseconds as in the case of the QCD corrections, see ref. [16].

4.3 Comparison to ref. [11]

In this section we compare our results for the form factors with the numerical evaluations of ref. [11]. By comparing eqs. (2.14)-(2.16) of ref. [11] with our definitions in eqs. (2.8) and (2.9), we can establish relations between the two form factor definitions, which are given by

$$F^{(0)}_{g_t^2,\text{box}} = -\frac{s}{32\,m_t^2\,\pi^2}\,F^{(0)}_{\text{box}} \tag{4.3}$$

JHEP04(2025)193

at one loop and

$$
\begin{aligned}
F^{(1)}_{g_t^4,\text{box}} &= -\frac{s\, e^{-2\gamma_E \epsilon}}{64\, m_t^2\, \pi^4} \left(\frac{\mu^2}{4\pi\, m_t^2}\right)^{-2\epsilon} F^{(0,y_t^4)}_{\text{box}}\,, \\
F^{(1)}_{g_t^2\, g_3^2,\text{box}} &= -\frac{s}{576\, m_H^2\, m_t^2\, \pi^4}\, F^{(0,y_t^2\, g_3^2)}_{\text{box}}\,, \\
F^{(1)}_{g_t^3\, g_3,\text{box}} &= -\frac{s}{192\, m_H\, m_t^2\, \pi^4}\, F^{(0,y_t^3\, g_3)}_{\text{box}}\,, \\
F^{(1)}_{g_t^2\, g_4,\text{box}} &= -\frac{s}{192\, m_t^2\, \pi^4}\, F^{(0,y_t^2\, g_4)}_{\text{box}}
\end{aligned}
\tag{4.4}
$$

at two loops. Here we have omitted the subscript $i = 1, 2$ which denotes the two Lorentz projections of the structures in eq. (2.2), and added the subscript "box" to the form factors on the left-hand side since we do not consider triangle diagrams in the comparison. We also do not compare one-loop results since the quality of their high-energy expansions is discussed in ref. [16]. Note that $F^{(0,y_t^4)}_{\text{box}}$ is divergent, thus its conversion factor is ϵ dependent. Some conversion factors are dimensionful because our form factors are dimensionless and some of those of ref. [11] are not.

While in section 4.2 we have used $\mu^2 = s$, we compare with data for the form factors of ref. [11][2] for $\mu^2 = m_t^2$ and thus adopt that choice here. Similarly we use common mass values of $m_t = 173.055\,\text{GeV}$ and $m_H = 125\,\text{GeV}$.

In figures 9–12 we compare our results and the numerically evaluated form factors for the four two-loop form factors of eq. (4.4). We show the comparison both as a function of the final-state Higgs boson transverse momentum p_T and as a function of $\sqrt{s}$. The uncertainties displayed in the plots are due to our uncertainties and those of ref. [11], combined in quadrature. We show data points for values of $p_T \geq 300\,\text{GeV}$, which imply a $\sqrt{s}$ value of at least 650 GeV. In this region our Padé uncertainties are extremely small; the uncertainties visible in the plots are therefore almost entirely due to the numerical integration. The exception to this is $F^{(0,y_t^3\, g_3)}_{\text{box1}}$, where our Padé uncertainties dominate for smaller values of p_T. In the case of the real part there are only a few data points with uncertainties. Those with $p_T < 500\,\text{GeV}$ and $\sqrt{s} < 1000\,\text{GeV}$ are dominated by the Padé uncertainty. In the case of the imaginary part all uncertainties below $p_T = 470\,\text{GeV}$ or $\sqrt{s} = 1300\,\text{GeV}$ basically come from the Padé approach.

In the plots we show several sets of data points. The light blue and yellow points in the left-hand column show the form factor values for our expansions and from ref. [11], respectively. In the central and right-hand columns we show the differences and relative differences between ref. [11] and our expansions truncated at various orders: the red, orange, dark blue and dark green points include terms to orders $m_H^4\,\delta^3$, $m_H^4\,\delta^1$, $m_H^4\,\delta^2$ and $m_H^2\,\delta^3$ respectively. Thus the red points display our best approximation.

Figure 9 shows the comparison for the real and imaginary finite parts of the (bare) form factor $F^{(0,y_t^4)}_{\text{box1}}$. We find good agreement between our expansions and the numerical evaluations of ref. [11]; that is, the difference or relative difference between the data points is consistent with zero within the uncertainties and the relative difference has a typical value below about 1% and 0.5% for the real and imaginary parts, respectively. The differences in

[2]We would like to thank the authors of ref. [11] for providing this data, by private communication.

JHEP04(2025)193

values are both positive and negative, suggesting agreement up to the (Gaussian distributed) numerical integration uncertainties.

Figure 10 shows the comparison for the real and imaginary parts of the form factor $F^{(0,y_t^2\,g_3^2)}_{\text{box1}}$. Here, though the difference between our results is small in an absolute sense, the relative difference is inflated due to the small absolute value of the form factor and its zero crossing. Here we observe that our results are not consistent with the numerical evaluation within the uncertainties but rather show a systematic offset from the values of ref. [11] at a level below about 2% or better, which we attribute to the truncation of our expansions at $m_H^4\,\delta^3$. The comparison of the imaginary part (lower two rows) is qualitatively rather similar, however the larger values of the form factor itself leads to a smaller relative difference of about 1% or better. The comparison of the real part of $F^{(0,y_t^3\,g_3)}_{\text{box1}}$ in figure 11 also displays the same systematic offset from the numerical evaluation due to the truncation of our expansion and a broadly similar relative difference of about 2% or better.

On the other hand, the imaginary part of $F^{(0,y_t^3\,g_3)}_{\text{box1}}$ (shown in the lower two rows of figure 11) is not well controlled by our expansion for $p_T \lesssim 500\text{GeV}$. In contrast to the other plots of this section, here the error bars are dominated by the uncertainty estimate of our Padé procedure. For $p_T \gtrsim 500\text{GeV}$ we observe the same $1-2\%$-level agreement as for the other form factors. This form factor contains contributions from the poorly-performing I_{157} and I_{164} master integrals discussed in section 4.1.

Finally, in figure 12 we compare values of $F^{(0,y_t^2\,g_4)}_{\text{box1}}$. The quartic self-coupling of the Higgs boson means that this form factor has "$2 \to 1$" kinematics and is thus independent of p_T (or t and u). This leads to excellent agreement at a level below 0.5%, since there are no kinematic cuts which can spoil the validity of our results above $\sqrt{s} = 3\,m_t$.

While we have only discussed the F_{box1} form factors here for brevity, the F_{box2} form factors show approximately the same level of agreement with the numerical evaluations of ref. [11]. That is, agreement at the $1-2\%$ level for $F^{(0,y_t^4)}_{\text{box2}}$ and $F^{(0,y_t^2\,g_3^2)}_{\text{box2}}$, and agreement for $F^{(0,y_t^3\,g_3)}_{\text{box2}}$ only in the region $p_T \gtrsim 500\,\text{GeV}$.

JHEP04(2025)193

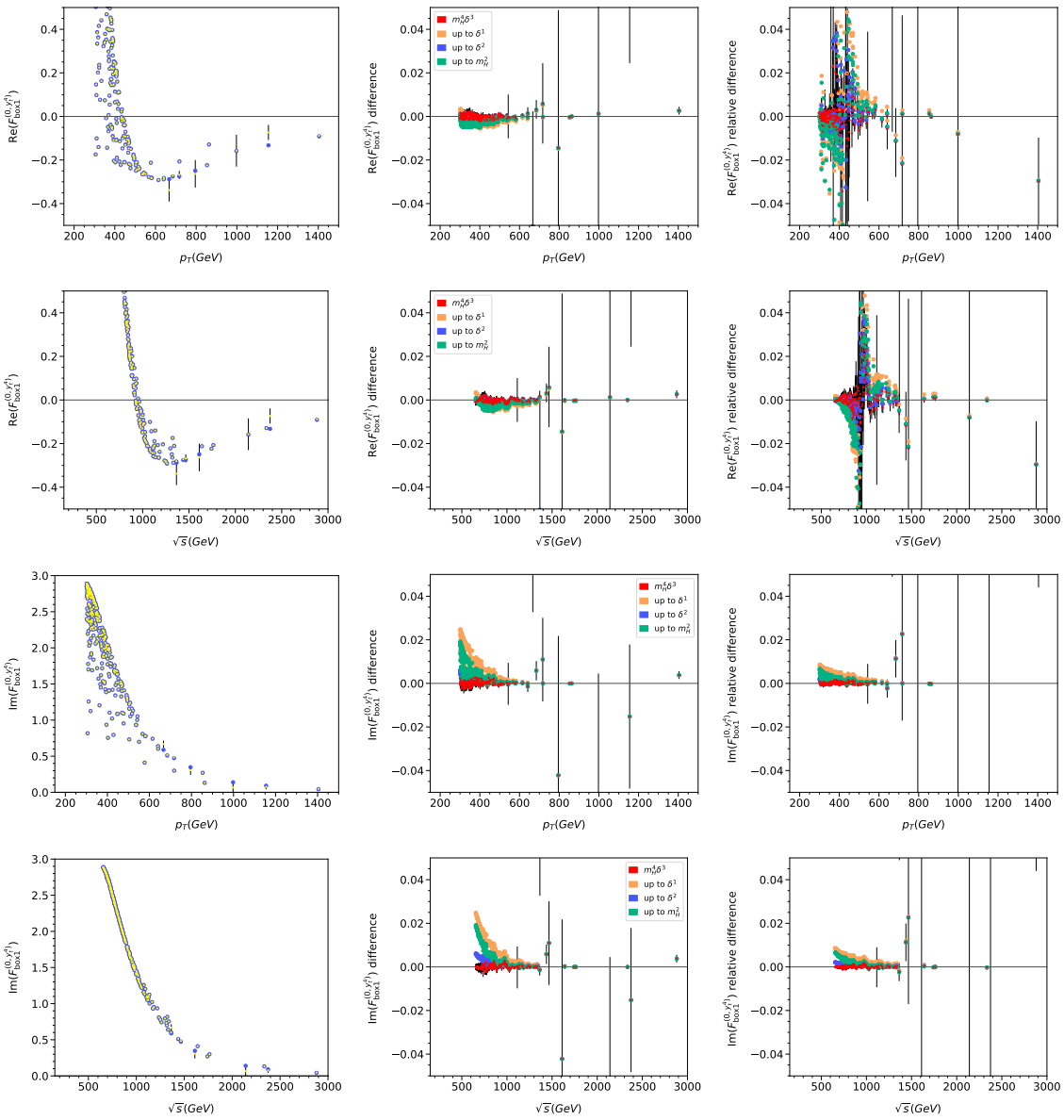

Figure 9. $F^{(0,y_t^4)}_{\text{box1}}$ form factor (left column), absolute (middle column) and relative (right column) difference compared to ref. [11]. We show the real (upper two rows) and imaginary (lower two rows) parts as a function of p_T and of $\sqrt{s}$. We show phase-space points with a p_T value of at least 300GeV. The data point colours are as defined in the text.

JHEP04(2025)193

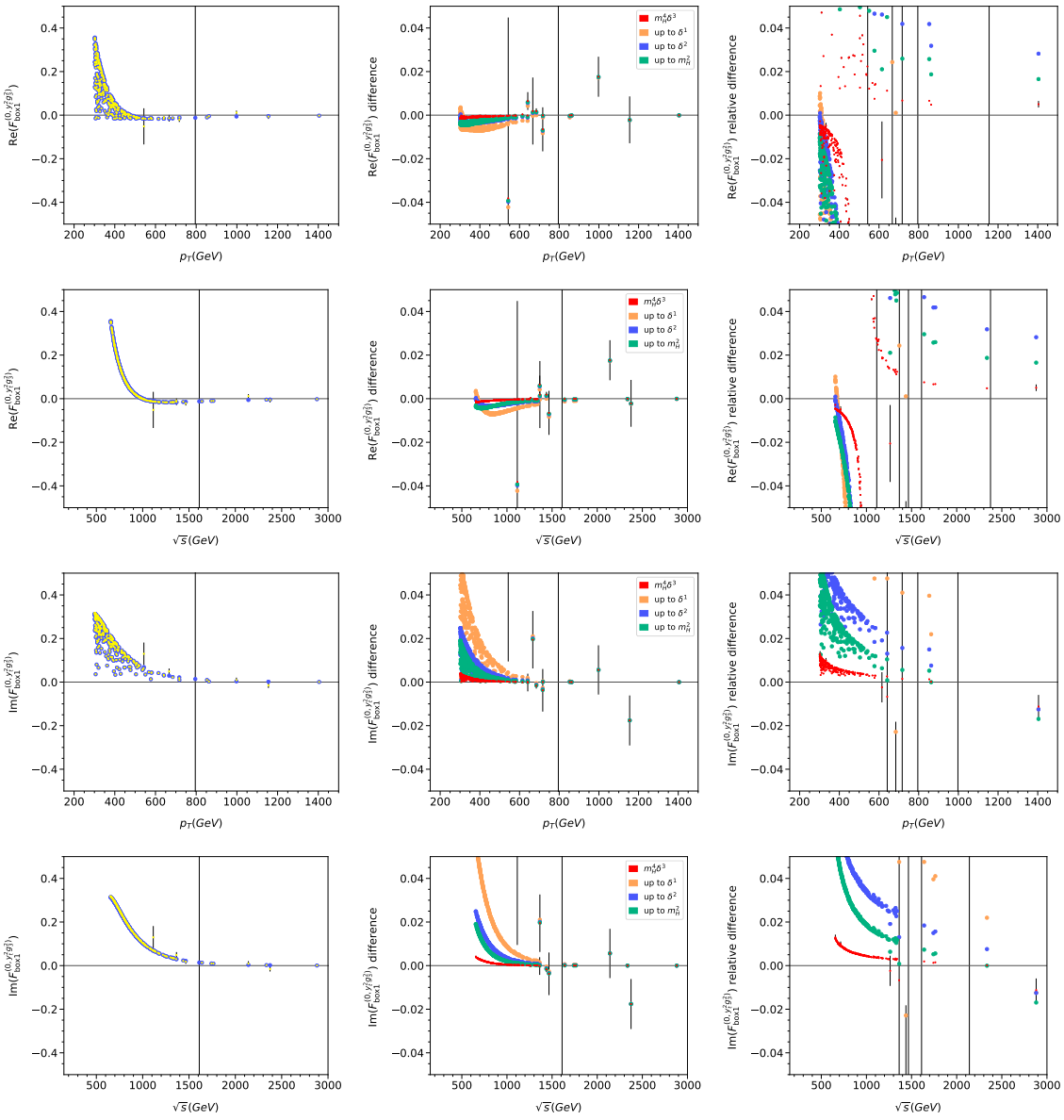

Figure 10. As figure 9, for $F^{(0,y_t^2\,g_3^2)}_{\text{box1}}$.

JHEP04(2025)193

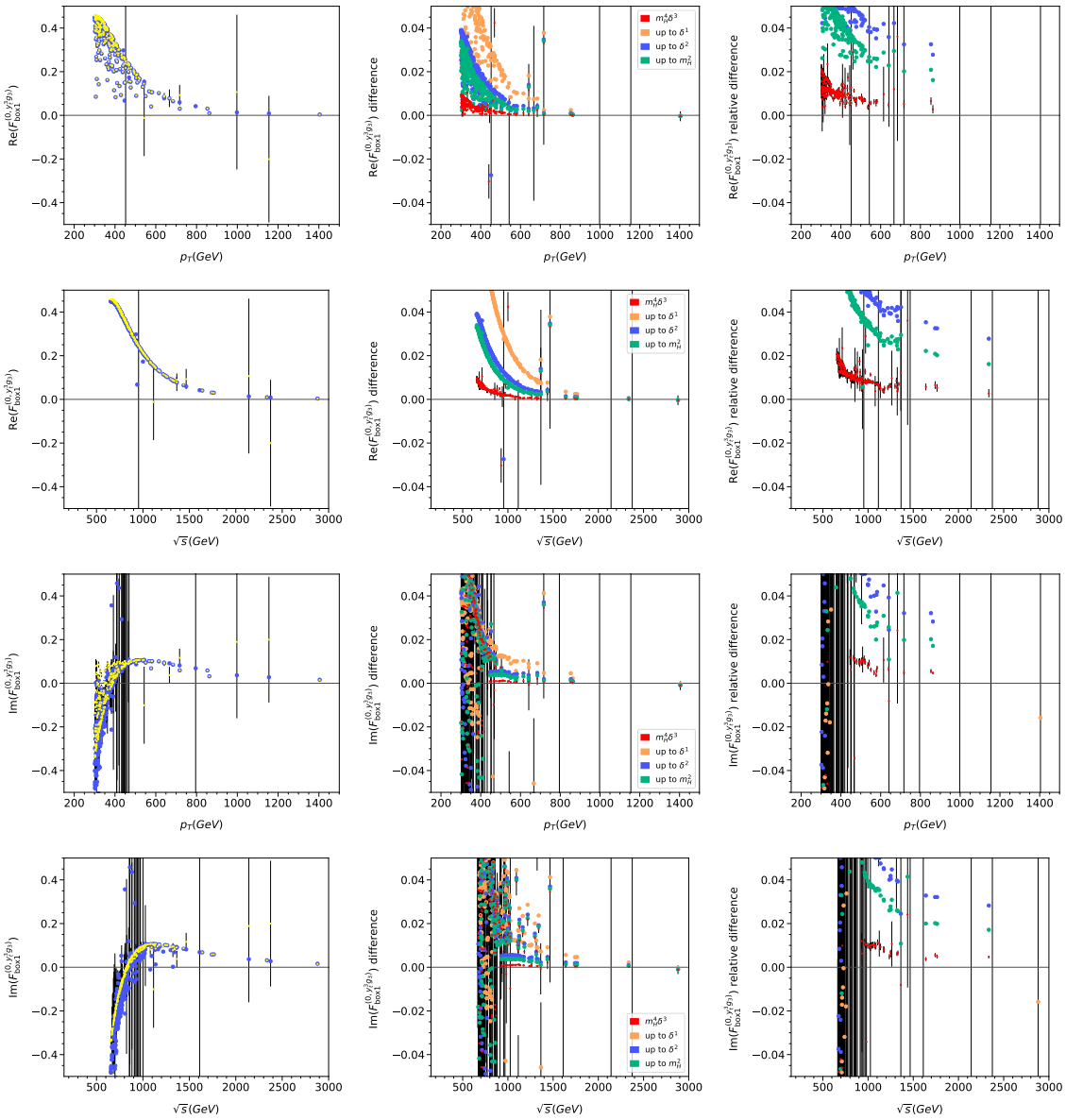

Figure 11. As figure 9, for $F^{(0,y_t^3\, g_3)}_{\text{box1}}$.

JHEP04(2025)193

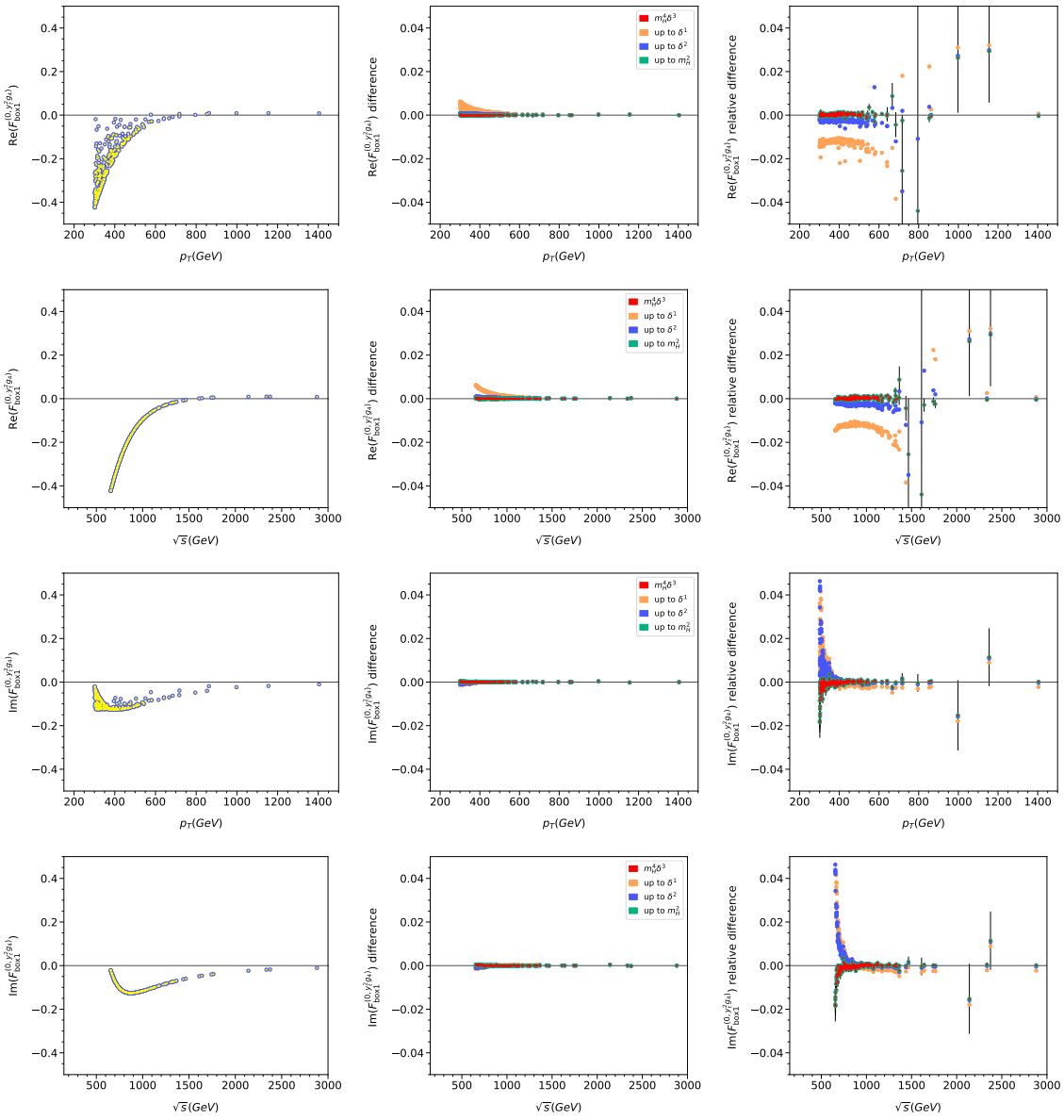

Figure 12. As figure 9, for $F_{\text{box1}}^{(0,y_t^2\,g_4)}$.

JHEP04(2025)193

5 Conclusions and outlook

Analytic expansions in different regions in phase space constitute a complementary approach to purely numerical evaluations of master integrals. In this paper we compute the high-energy expansion of the master integrals needed for the NLO electroweak corrections to Higgs boson pair production in gluon fusion. First we perform Taylor expansions in the final-state Higgs mass and in the difference of the top quark and internal-Higgs boson masses, including three and four terms respectively. This leads to fully-massive two-loop box integrals where all external lines are massless. Applying an asymptotic expansion and exploiting the differential equations for the master integrals we expand them for small top quark mass and compute more than 100 expansion terms. This is the main result of the paper and the results can be downloaded from [55].

The master integrals are used to compute analytic results for all box-like form factors for $gg \to HH$ which contain Higgs and top quark propagators. For this subset the renormalization is particularly simple: all but one form factors are finite; for the contribution with four Yukawa couplings, which has already been treated in ref. [6], only the top quark mass has to be renormalized.

For the numerical evaluation of the form factors we apply a Padé approximation procedure which improves convergence for smaller values of p_T and $\sqrt{s}$. For most of the form factors we obtain precise results for $p_T \gtrsim 300\,\text{GeV}$ and the uncertainties remain small even for smaller values of p_T, see also discussion in refs. [6, 16]. The exception is the imaginary part of $F_{\text{box1}}^{(0,y_t^3 g_3)}$, which is only well approximated for $p_T \gtrsim 500\,\text{GeV}$. From the detailed comparison with the numerical results from ref. [11] we estimate that the remaining uncertainty due to the expansion in δ and m_H^{ext} is at most of the order of 1–2%.

We mention that our analytic calculation produces fairly large expressions in intermediate steps. However, the final numerical evaluation, which includes the construction of $\mathcal{O}(10-100)$ Padé results, is very fast. This is a crucial advantage as compared to the numerical approach, allowing the easy evaluation of additional phase space points and the ability to adjust mass values.

The master integrals computed in this paper together with the deep high-energy expansion of the QCD master integrals from refs. [13, 14] are sufficient to compute the complete top quark mass-induced Standard Model electroweak corrections in the high-energy limit. Furthermore, it will be interesting to compute the amplitude in the forward scattering limit such that the combination of both analytic expansions covers the whole phase space. These investigations are subject to ongoing work.

Acknowledgments

The work was supported by the Deutsche Forschungsgemeinschaft (DFG, German Research Foundation) under grant 396021762 — TRR 257 "Particle Physics Phenomenology after the Higgs Discovery", the European Research Council (ERC) under the European Union's Horizon 2020 research and innovation programme grant agreement 101019620 (ERC Advanced Grant TOPUP), the UZH Postdoc Grant, grant no. [FK-24-115], the Swiss National Science Foundation (SNSF) under contract TMSGI2 211209, and the STFC Consolidated Grant

JHEP04(2025)193

ST/X000699/1. We would like to thank the authors of ref. [11] for providing the data in section 4.3 by private communication.

Data Availability Statement. This article has associated data in a data repository.

Code Availability Statement. This article has no associated code or the code will not be deposited.

JHEP04(2025)193

References

[1] S. Borowka et al., *Higgs Boson Pair Production in Gluon Fusion at Next-to-Leading Order with Full Top-Quark Mass Dependence*, *Phys. Rev. Lett.* **117** (2016) 012001 [*Erratum ibid.* **117** (2016) 079901] [arXiv:1604.06447] [INSPIRE].

[2] S. Borowka et al., *Full top quark mass dependence in Higgs boson pair production at NLO*, *JHEP* **10** (2016) 107 [arXiv:1608.04798] [INSPIRE].

[3] J. Baglio et al., *Gluon fusion into Higgs pairs at NLO QCD and the top mass scheme*, *Eur. Phys. J. C* **79** (2019) 459 [arXiv:1811.05692] [INSPIRE].

[4] J. Davies et al., *Double Higgs boson production at NLO: combining the exact numerical result and high-energy expansion*, *JHEP* **11** (2019) 024 [arXiv:1907.06408] [INSPIRE].

[5] M. Mühlleitner, J. Schlenk and M. Spira, *Top-Yukawa-induced corrections to Higgs pair production*, *JHEP* **10** (2022) 185 [arXiv:2207.02524] [INSPIRE].

[6] J. Davies et al., *Higgs boson contribution to the leading two-loop Yukawa corrections to $gg \to HH$*, *JHEP* **08** (2022) 259 [arXiv:2207.02587] [INSPIRE].

[7] J. Davies, K. Schönwald, M. Steinhauser and H. Zhang, *Next-to-leading order electroweak corrections to $gg \to HH$ and $gg \to gH$ in the large-m_t limit*, *JHEP* **10** (2023) 033 [arXiv:2308.01355] [INSPIRE].

[8] H.-Y. Bi et al., *Electroweak Corrections to Double Higgs Production at the LHC*, *Phys. Rev. Lett.* **132** (2024) 231802 [arXiv:2311.16963] [INSPIRE].

[9] H. Zhang, K. Schönwald, M. Steinhauser and J. Davies, *Electroweak corrections to $gg \to HH$: Factorizable contributions*, *PoS* **LL2024** (2024) 014 [arXiv:2407.05787] [INSPIRE].

[10] S. Borowka et al., *Probing the scalar potential via double Higgs boson production at hadron colliders*, *JHEP* **04** (2019) 016 [arXiv:1811.12366] [INSPIRE].

[11] G. Heinrich et al., *Electroweak corrections to Higgs boson pair production: the top-Yukawa and self-coupling contributions*, *JHEP* **11** (2024) 040 [arXiv:2407.04653] [INSPIRE].

[12] H.T. Li et al., *Improved constraints on Higgs boson self-couplings with quartic and cubic power dependencies of the cross section*, *Chin. Phys. C* **49** (2025) 023107 [arXiv:2407.14716] [INSPIRE].

[13] J. Davies, G. Mishima, M. Steinhauser and D. Wellmann, *Double-Higgs boson production in the high-energy limit: planar master integrals*, *JHEP* **03** (2018) 048 [arXiv:1801.09696] [INSPIRE].

[14] J. Davies, G. Mishima, M. Steinhauser and D. Wellmann, *Double Higgs boson production at NLO in the high-energy limit: complete analytic results*, *JHEP* **01** (2019) 176 [arXiv:1811.05489] [INSPIRE].

[15] L. Bellafronte et al., *Gluon fusion production at NLO: merging the transverse momentum and the high-energy expansions*, *JHEP* **07** (2022) 069 [arXiv:2202.12157] [INSPIRE].

[16] J. Davies, G. Mishima, K. Schönwald and M. Steinhauser, *Analytic approximations of $2 \to 2$ processes with massive internal particles*, *JHEP* **06** (2023) 063 [arXiv:2302.01356] [INSPIRE].

[17] J. Davies, G. Mishima and M. Steinhauser, *Virtual corrections to $gg \to ZH$ in the high-energy and large-m_t limits*, *JHEP* **03** (2021) 034 [arXiv:2011.12314] [INSPIRE].

[18] J. Davies, G. Mishima, M. Steinhauser and D. Wellmann, *$gg \to ZZ$: analytic two-loop results for the low- and high-energy regions*, *JHEP* **04** (2020) 024 [arXiv:2002.05558] [INSPIRE].

[19] G. Degrassi, R. Gröber, M. Vitti and X. Zhao, *On the NLO QCD corrections to gluon-initiated ZH production*, *JHEP* **08** (2022) 009 [arXiv:2205.02769] [INSPIRE].

[20] L. Chen et al., *ZH production in gluon fusion at NLO in QCD*, *JHEP* **08** (2022) 056 [arXiv:2204.05225] [INSPIRE].

[21] G. Degrassi, R. Gröber and M. Vitti, *Virtual QCD corrections to $gg \to ZZ$: top-quark loops from a transverse-momentum expansion*, *JHEP* **07** (2024) 244 [arXiv:2404.15113] [INSPIRE].

[22] S. Jaskiewicz, S. Jones, R. Szafron and Y. Ulrich, *The structure of quark mass corrections in the $gg \to HH$ amplitude at high-energy*, arXiv:2501.00587 [INSPIRE].

[23] P. Nogueira, *Automatic Feynman Graph Generation*, *J. Comput. Phys.* **105** (1993) 279 [INSPIRE].

[24] M. Gerlach, F. Herren and M. Lang, *tapir: A tool for topologies, amplitudes, partial fraction decomposition and input for reductions*, *Comput. Phys. Commun.* **282** (2023) 108544 [arXiv:2201.05618] [INSPIRE].

[25] B. Ruijl, T. Ueda and J. Vermaseren, *FORM version 4.2*, arXiv:1707.06453 [INSPIRE].

[26] R. Harlander, T. Seidensticker and M. Steinhauser, *Complete corrections of Order alpha alpha-s to the decay of the Z boson into bottom quarks*, *Phys. Lett. B* **426** (1998) 125 [hep-ph/9712228] [INSPIRE].

[27] T. Seidensticker, *Automatic application of successive asymptotic expansions of Feynman diagrams*, in the proceedings of the *6th International Workshop on New Computing Techniques in Physics Research: Software Engineering, Artificial Intelligence Neural Nets, Genetic Algorithms, Symbolic Algebra, Automatic Calculation*, Heraklion, Greece, April 12–16 (1999) [hep-ph/9905298] [INSPIRE].

[28] M. Fael, K. Schönwald and M. Steinhauser, *A first glance to the kinematic moments of $B \to X_c \ell \nu$ at third order*, *JHEP* **08** (2022) 039 [arXiv:2205.03410] [INSPIRE].

[29] R.N. Lee, *Presenting LiteRed: a tool for the Loop InTEgrals REDuction*, arXiv:1212.2685 [INSPIRE].

[30] R.N. Lee, *LiteRed 1.4: a powerful tool for reduction of multiloop integrals*, *J. Phys. Conf. Ser.* **523** (2014) 012059 [arXiv:1310.1145] [INSPIRE].

[31] P. Maierhöfer, J. Usovitsch and P. Uwer, *Kira — A Feynman integral reduction program*, *Comput. Phys. Commun.* **230** (2018) 99 [arXiv:1705.05610] [INSPIRE].

[32] J. Klappert, F. Lange, P. Maierhöfer and J. Usovitsch, *Integral reduction with Kira 2.0 and finite field methods*, *Comput. Phys. Commun.* **266** (2021) 108024 [arXiv:2008.06494] [INSPIRE].

JHEP04(2025)193

[33] G. Mishima, *High-Energy Expansion of Two-Loop Massive Four-Point Diagrams*, *JHEP* **02** (2019) 080 [arXiv:1812.04373] [INSPIRE].

[34] J. Klappert and F. Lange, *Reconstructing rational functions with FireFly*, *Comput. Phys. Commun.* **247** (2020) 106951 [arXiv:1904.00009] [INSPIRE].

[35] J. Klappert, S.Y. Klein and F. Lange, *Interpolation of dense and sparse rational functions and other improvements in FireFly*, *Comput. Phys. Commun.* **264** (2021) 107968 [arXiv:2004.01463] [INSPIRE].

[36] H. Zhang, *Massive two-loop four-point Feynman integrals at high energies with AsyInt*, *JHEP* **09** (2024) 069 [arXiv:2407.12107] [INSPIRE].

[37] B. Jantzen, A.V. Smirnov and V.A. Smirnov, *Expansion by regions: revealing potential and Glauber regions automatically*, *Eur. Phys. J. C* **72** (2012) 2139 [arXiv:1206.0546] [INSPIRE].

[38] M. Czakon, *Automatized analytic continuation of Mellin-Barnes integrals*, *Comput. Phys. Commun.* **175** (2006) 559 [hep-ph/0511200] [INSPIRE].

[39] J. Blümlein and S. Kurth, *Harmonic sums and Mellin transforms up to two loop order*, *Phys. Rev. D* **60** (1999) 014018 [hep-ph/9810241] [INSPIRE].

[40] J.A.M. Vermaseren, *Harmonic sums, Mellin transforms and integrals*, *Int. J. Mod. Phys. A* **14** (1999) 2037 [hep-ph/9806280] [INSPIRE].

[41] J. Blümlein, *Structural Relations of Harmonic Sums and Mellin Transforms up to Weight $w = 5$*, *Comput. Phys. Commun.* **180** (2009) 2218 [arXiv:0901.3106] [INSPIRE].

[42] J. Ablinger, *A Computer Algebra Toolbox for Harmonic Sums Related to Particle Physics*, M.Sc. thesis, Linz University, Austria (2009) [arXiv:1011.1176] [INSPIRE].

[43] J. Ablinger, J. Blümlein and C. Schneider, *Harmonic Sums and Polylogarithms Generated by Cyclotomic Polynomials*, *J. Math. Phys.* **52** (2011) 102301 [arXiv:1105.6063] [INSPIRE].

[44] J. Ablinger, *Computer Algebra Algorithms for Special Functions in Particle Physics*, Ph.D. thesis, Linz University, Austria (2012) [arXiv:1305.0687] [INSPIRE].

[45] J. Ablinger, J. Blümlein and C. Schneider, *Generalized Harmonic, Cyclotomic, and Binomial Sums, their Polylogarithms and Special Numbers*, *J. Phys. Conf. Ser.* **523** (2014) 012060 [arXiv:1310.5645] [INSPIRE].

[46] J. Ablinger, J. Blümlein and C. Schneider, *Analytic and Algorithmic Aspects of Generalized Harmonic Sums and Polylogarithms*, *J. Math. Phys.* **54** (2013) 082301 [arXiv:1302.0378] [INSPIRE].

[47] J. Ablinger, J. Blümlein, C.G. Raab and C. Schneider, *Iterated Binomial Sums and their Associated Iterated Integrals*, *J. Math. Phys.* **55** (2014) 112301 [arXiv:1407.1822] [INSPIRE].

[48] J. Ablinger, *The package HarmonicSums: Computer Algebra and Analytic aspects of Nested Sums*, *PoS* **LL2014** (2014) 019 [arXiv:1407.6180] [INSPIRE].

[49] J. Ablinger, *Discovering and Proving Infinite Binomial Sums Identities*, *Exper. Math.* **26** (2016) 62 [arXiv:1507.01703] [INSPIRE].

[50] J. Ablinger, *Computing the Inverse Mellin Transform of Holonomic Sequences using Kovacic's Algorithm*, *PoS* **RADCOR2017** (2018) 001 [arXiv:1801.01039] [INSPIRE].

[51] C. Schneider, *Symbolic summation assists combinatorics*, *Sem. Lothar. Combin.* **56** (2007) 1.

[52] C. Schneider, *Term Algebras, Canonical Representations and Difference Ring Theory for Symbolic Summation*, arXiv:2102.01471.

JHEP04(2025)193

[53] H.R.P. Ferguson, D.H. Bailey and S. Arno, *Analysis of pslq, an integer relation finding algorithm*, *Math. Comput.* **68** (1999) 351.

[54] J. Ablinger et al., *Automated Solution of First Order Factorizable Systems of Differential Equations in One Variable*, *Nucl. Phys. B* **939** (2019) 253 [arXiv:1810.12261] [INSPIRE].

[55] https://www.ttp.kit.edu/preprints/2025/ttp25-001/.

[56] A.B. Goncharov, *Multiple polylogarithms, cyclotomy and modular complexes*, *Math. Res. Lett.* **5** (1998) 497 [arXiv:1105.2076] [INSPIRE].

[57] J.M. Henn, A.V. Smirnov and V.A. Smirnov, *Evaluating Multiple Polylogarithm Values at Sixth Roots of Unity up to Weight Six*, *Nucl. Phys. B* **919** (2017) 315 [arXiv:1512.08389] [INSPIRE].

[58] X. Liu and Y.-Q. Ma, *AMFlow: A Mathematica package for Feynman integrals computation via auxiliary mass flow*, *Comput. Phys. Commun.* **283** (2023) 108565 [arXiv:2201.11669] [INSPIRE].

[59] X. Liu, Y.-Q. Ma and C.-Y. Wang, *A Systematic and Efficient Method to Compute Multi-loop Master Integrals*, *Phys. Lett. B* **779** (2018) 353 [arXiv:1711.09572] [INSPIRE].

JHEP04(2025)193